



Cite this: *Phys. Chem. Chem. Phys.*,
2024, 26, 21099

Ab initio electronic structure analysis of ground and excited states of $\text{HfN}^{0,+,\ddagger}$

Isuru R. Ariyaratna *

High-level *ab initio* electronic structure analysis of third-row transition metal (TM)-based diatomic species is challenging and has been perpetually lagging. In this work, fourteen and eighteen electronic states of HfN and HfN^+ respectively are studied, employing multireference configuration interaction (MRCI) and coupled cluster singles doubles and perturbative triples [CCSD(T)] theories under larger correlation-consistent basis sets. Their potential energy curves (PECs), energetics, and spectroscopic parameters are reported. Core electron correlation effects on their properties are also investigated. Chemical bonding patterns of several low-lying electronic states are introduced based on the equilibrium electron configurations. The ground state of HfN ($X^2\Sigma^+$) has the $1\sigma^2 2\sigma^2 3\sigma^1 1\pi^4$ electronic configuration, and the ionization of the $3\sigma^1$ electron produces the ground state of HfN^+ ($X^1\Sigma^+$). Ground states of both HfN and HfN^+ are triple bonded in nature and bear 124.86 and 109.10 kcal mol⁻¹ binding energies with respect to their ground state fragments. The findings of this work agree well with the limited experimental literature available and provide useful reference values for future experimental analysis of HfN and HfN^+ .

Received 3rd May 2024,
Accepted 16th July 2024

DOI: 10.1039/d4cp01847h

rsc.li/pccp

1. Introduction

Today, scientists are making great advances in synthesizing and characterizing a variety of TM-based molecular systems with novel or improved chemicophysical properties for applications in electronics, catalysis, pharmaceuticals, and many other industrial fields. Indeed, chemical bonding is the basis that allows for a particular molecular structure to exist and permits geometrical manipulations to synthesize desired complexes. Hence, understanding the nature of the chemical bonding is vital. Utilization of high-level theoretical tools for gaining insight on electronic structures and bonding of molecular systems is rather common. However, such theoretical studies of TM-based systems are challenging due to their complicated electronic structures. Especially, bonding analysis of TM-based diatomic species is demanding owing to their many closely lying electronic structures, multireference characteristics of the states, and the dependence of results on the level of theory utilized.^{1,2}

Over the years, several attempts have been made to demystify the chemical bonding of TM monoxides primarily aiming to

investigate the oxidation process of TM surfaces and to understand and predict catalytic properties of TM oxides.^{1,3–7} Of course, investigation of TM nitrides (or TM–N bond) is equally important because of their applications in various fields. For example, TM nitride systems are being applied as electrochemical energy storage materials,⁸ coating materials,^{9,10} dielectrics, semiconductors, and electrical conductors.¹¹ Furthermore, they are potential electrocatalysts for water splitting reactions^{12,13} and are also being tested as photocatalysts.^{14,15} So far, *ab initio* electronic structure analysis of ground and excited states of all first-row (Sc–Cu)¹ and several second-row TMs mononitrides (Y–Rh)^{16–23} have been reported. Relatively, such studies are scarce for third-row TM mononitrides and hence this work is devoted to high-level *ab initio* analysis of the third-row TM mononitride HfN and its cation.

The first bonding analysis of HfN goes back to Karl Gingerich's work in 1968 of analyzing bond energies of HfN .²⁴ This study estimated a 141 kcal mol⁻¹ D_0 for HfN . In 1973, Kohl and Stearns identified HfN by a molecular beam mass spectrometric study and reported a D_0 of 126.83(7.15) kcal mol⁻¹ for HfN .²⁵ Six years later, DeVore and Gallaher performed a vibrational infrared spectroscopic analysis for HfN and determined its harmonic vibrational frequency (ω_e) and bond distance (r_e) to be 919.5(20) cm⁻¹ and 1.69(30) Å, respectively.²⁶ Furthermore, based on the spectral features, they predicted a $^2\Sigma^+$ ground state for the molecule.²⁶ In 1997, Ram and Bernath carried out a Fourier transform infrared spectroscopic analysis to investigate the electronic emission spectrum of HfN and observed a set of bands in the 5500–6800 cm⁻¹ region that corresponds to the $[6.7]^2\Sigma^+ - X^2\Sigma^+$ transition.²⁷ Furthermore, they reported a r_e of 1.724678(36) Å,

Physics and Chemistry of Materials (T-1), Los Alamos National Laboratory, Los Alamos, NM 87545, USA. E-mail: isuru@lanl.gov

† Electronic supplementary information (ESI) available: Table S1 lists the molecular orbital compositions of HfN ; Table S2 lists spectroscopic constants and compositions of low-lying spin–orbit state of HfN ; Table S3 lists the D_e , r_e , ω_e , and $\omega_e x_e$ values of the $\text{HfN}(X^2\Sigma^+)$ and $\text{HfN}^+(X^1\Sigma^+)$ at the TZ-C-CCSD(T) level; Table S4 lists spectroscopic constants and compositions of low-lying spin–orbit state of HfN^+ ; Fig. S1 illustrates the DMCs of low-lying electronic states of HfN^+ . See DOI: <https://doi.org/10.1039/d4cp01847h>



ω_e of 932.7164(15) cm^{-1} , and anharmonicity ($\omega_e x_e$) of 4.41299(65) cm^{-1} for HfN.²⁷ Importantly, they highlighted the fact that more experimental and theoretical analyses are necessary to understand low-lying states of HfN, but twenty-seven years since their discovery, this system still remains poorly understood. In 1999 Kushto *et al.*²⁸ performed density functional theory (DFT) BP86 calculations for HfN, and their r_e (1.734 Å) and ω_e (942 cm^{-1}) values are in reasonable agreement with the findings of Ram and Bernath.²⁷ Another DFT/B3LYP study carried out by Hong *et al.*,²⁹ reported a dissociation energy (D_e) of 113.92 kcal mol^{-1} , ω_e of 940 cm^{-1} , r_e of 1.764 Å, ionization energy (IE) of 7.7 eV, and dipole moment (μ) of 5.70 D for HfN. Furthermore, under the same level of theory, they reported corresponding values for HfN⁺ (*i.e.*, D_e of 91.55 kcal mol^{-1} , ω_e of 994 cm^{-1} , r_e of 1.720 Å, and μ of 6.18 D).²⁹ The most recent work on HfN is reported by the Morse group.³⁰ They measured the D_0 of HfN to be 123.93(9) kcal mol^{-1} using resonant two-photon ionization spectroscopy.³⁰ Furthermore, they performed CCSD(T) analysis for HfN and the calculated D_0 value at the complete basis set (CBS) limit is 127.99 kcal mol^{-1} .³⁰

In the present work, ground and excited electronic states of HfN and HfN⁺ were studied utilizing the *ab initio* MRCI, MRCI+Q, and CCSD(T) theories to shed light on their PECs, equilibrium electronic configurations, chemical bonding patterns, and D_e , r_e , T_e , ω_e , $\omega_e x_e$, and μ values. The basis set effects, core electron correlation effects, spin-orbit effects on the energy related properties and spectroscopic parameters are also reported.

II. Computational details

The MOLPRO 2023.2 quantum chemistry package was utilized for all calculations.^{31–33} In all cases, C_{2v} Abelian sub point group of the original $C_{\infty v}$ non-Abelian symmetries of HfN and HfN⁺ was used. First, full PECs of fourteen and eighteen low-lying electronic states of HfN and HfN⁺ respectively were produced at the internally contracted MRCI^{34–36} level using the correlation consistent aug-cc-pVQZ of N³⁷ and cc-pVQZ-PP of Hf³⁸ basis set. For Hf, the Stuttgart relativistic pseudopotential that substitutes $1s^2 2s^2 2p^6 3s^2 3p^6 4s^2 3d^{10} 4p^6 4d^{10} 4f^{14}$ electrons was used (ECP60).³⁸ Complete active space self-consistent field (CASSCF)^{39–42} reference wavefunctions (WFs) were provided for MRCI calculations. Specifically, the CAS(7,12) (7 electrons in 12 orbitals) and CAS(6,12) (6 electrons in 12 orbitals) active spaces were used for HfN and HfN⁺, respectively. When the fragments are well separated (>10 Å), the CASSCF active orbitals are pure 6s, 6p, and 5d atomic orbitals of Hf and the 2p atomic orbitals of N. Under the utilized C_{2v} symmetry, they are $5a_1$ (6s, $5d_{z^2}$, $5d_{x^2-y^2}$, and $6p_z$ of Hf and $2p_z$ of N), $3b_1$ ($5d_{xz}$ and $6p_x$ of Hf and $2p_x$ of N), $3b_2$ ($5d_{yz}$ and $6p_y$ of Hf and $2p_y$ of N), and $1a_2$ ($5d_{xy}$ of Hf). The doubly occupied 2s atomic orbital of N is excluded from the CASSCF active space to achieve proper convergences. At the MRCI level, all valence electrons including the $2s^2$ of N were correlated. The Davidson correction (MRCI+Q) was used to reduce the size extensivity errors. The produced MRCI and MRCI+Q PECs of electronic states were used to

calculate each of their D_e , r_e , and T_e values. Furthermore, by solving the ro-vibrational Schrödinger equation numerically, ω_e and $\omega_e x_e$ values of the electronic states were calculated. The MRCI dipole moment curves (DMCs) of several low-lying states of HfN and HfN⁺ are also reported. Note that the negative μ values indicate that the positive and negative dipoles of the molecule are aligned with the negative and positive sides of the z-axis of the Cartesian coordinate plane. Spin-orbit coupling effects were evaluated at the MRCI level under the same basis set using the Breit–Pauli Hamiltonian as implemented in MOLPRO.

The CCSD(T)⁴³ potential energy scans were performed around the equilibrium bond distance regions of several low-lying single-reference electronic states of HfN and HfN⁺ using the same aug-cc-pVQZ of N³⁷ and cc-pVQZ-PP (60ECP) of Hf³⁸ basis set to obtain their D_e , r_e , T_e , ω_e and $\omega_e x_e$ values. To evaluate the effect of core electron correlation on the aforementioned properties of HfN and HfN⁺, another set of coupled cluster energy scans were carried out by correlating $5s^2 5p^6$ core electrons of Hf with the aug-cc-pVXZ of N³⁷ and cc-pwCVXZ-PP³⁸ (60ECP) of Hf basis set ($X = Q, 5$). Hereafter, these calculations are labelled as QZ-C-CCSD(T) or 5Z-C-CCSD(T). Similar C-CCSD(T) calculations were performed for the ground states of HfN and HfN⁺ at $X = T$ of aug-cc-pVXZ of N and cc-pwCVXZ-PP (60ECP) basis set [TZ-C-CCSD(T)], then the $X = T$, $X = Q$, and $X = 5$ PECs were extrapolated to the CBS limit to calculate CBS D_e , r_e , T_e , ω_e and $\omega_e x_e$ of HfN and HfN⁺. From now on the CBS extrapolated C-CCSD(T) approach is denoted by CBS-C-CCSD(T). The IE of HfN was also calculated under these coupled cluster methods. Coupled cluster, μ values of several single-reference electronic states of HfN and HfN⁺ were calculated using the finite-field method embedded in MOLPRO by applying a field of 0.01 a.u. Hartree–Fock wavefunctions were used for all coupled cluster calculations.

III. Results and discussion

III.A. HfN

The MRCI level of theory is ideal for calculating full PECs of highly correlated TM-based diatomic systems because of its ability to represent both single-reference and multireference electronic states accurately. Hence to study the electronic states of HfN, MRCI PECs originating from several low energy fragments of Hf + N were considered.

The ground state of Hf is an a^3F that carries $[Xe]4f^{14}5d^2 6s^2$ electronic configuration.⁴⁴ The $4f^{14}$ electrons of Hf are inert in nature but the four valence electrons ($5d^2 6s^2$ in ground state) and their excited configurations are known to readily participate in chemical reactions.^{7,45,46} The electron rearrangement within the 5d shell yields the first and second excited electronic states for Hf atom (*i.e.*, a^3P and a^1D) that lie ~ 16 – 26 kcal mol^{-1} and ~ 16 kcal mol^{-1} above, respectively.⁴⁴ The same $5d^2 6s^2$ electronic configuration is carried by its fourth excited state (*i.e.*, a^1G) that rests at ~ 30 kcal mol^{-1} .⁴⁴ The promotion of an electron from the 5d shell to the valence 6p orbitals creates its third and fifth excited state (*i.e.*, z^1D ; ~ 30 kcal mol^{-1} and z^3D ;



$\sim 40\text{--}53\text{ kcal mol}^{-1}$, respectively) with the $5d^16s^26p^1$ configuration.⁴⁴ Due to these diverse-types of low energy electronic states, we can expect the Hf + N reaction to produce a plethora of stable molecular electronic structures. In the present work, all the molecular electronic states arising from the interactions between the aforementioned states of Hf with the ground state of N (4S ; $[\text{He}]2s^22p^3$) were considered. The interaction between the excited electronic states of N *versus* the states of Hf were not studied since the excitation energies of N atom are relatively high. For example, the first excited state of N (2D) lies $\sim 54\text{ kcal mol}^{-1}$ high in energy which is even higher than the fifth excited state of Hf (z^3D).⁴⁴ The reactions between the $\text{Hf}(a^3F) + \text{N}(^4S)$, $\text{Hf}(a^3P) + \text{N}(^4S)$, $\text{Hf}(a^1D) + \text{N}(^4S)$, $\text{Hf}(z^1D) + \text{N}(^4S)$, $\text{Hf}(a^1G) + \text{N}(^4S)$, and $\text{Hf}(z^3D) + \text{N}(^4S)$ produce $^{2,4,6}(\Sigma^+, \Pi, \Delta, \Phi)$, $^{2,4,6}(\Sigma^+, \Pi)$, $^4(\Sigma^-, \Pi, \Delta)$, $^4(\Sigma^+, \Pi, \Delta)$, $^4(\Sigma^-, \Pi, \Delta, \Phi, \Gamma)$, and $^{2,4,6}(\Sigma^+, \Pi, \Delta)$ states, respectively. In this work, all these electronic states for HfN were studied at the CASSCF level to identify the most stable electronic states of HfN. Then, the fourteen most stable electronic states of HfN were investigated under the MRCI level of theory and are given in Fig. 1.

The right end of the potential energy profile of Fig. 1 represents the Hf + N fragments (a, b, c, d, e, and f). The PECs arising from the d- and e-fragments are not among the most stable fourteen electronic states of HfN and hence are not available in Fig. 1. Notice that at the MRCI level the $\text{Hf}(a^1D) + \text{N}(^4S)$ is slightly stabilized over the $\text{Hf}(a^3P) + \text{N}(^4S)$ (by $\sim 3\text{ kcal mol}^{-1}$) even though we expect the opposite based on the experimental excitation energies of Hf atom, where a^3P and a^1D are very closely lying first and second excited states of Hf, respectively.⁴⁴ All PECs produce minima around $1.7\text{--}1.9\text{ \AA}$ and are with $\sim 60\text{--}128\text{ kcal mol}^{-1}$ D_e with respect to the ground state fragments. The ground state of HfN is a $X^2\Sigma^+$ which dissociates to $\text{Hf}(a^3F) + \text{N}(^4S)$ ground state fragments. On the other hand, the first excited state of HfN ($2^2\Sigma^+$) dissociates to $\text{Hf}(a^3P) + \text{N}(^4S)$. The second excited state, $1^2\Pi$, lies closer to the $2^2\Sigma^+$ in energy (less than 5 kcal mol^{-1}) and originates from the ground state fragments. The first three electronic states of HfN lie well separated from the rest that are congested within the $60\text{--}90\text{ kcal mol}^{-1}$ energy range.

The equilibrium electronic configurations of the studied fourteen electronic states of HfN are reported in Table 1 and the corresponding state average CASSCF molecular orbitals are given in Fig. 2. The 1σ orbital (Fig. 2) is dominantly the polarized $2s$ of N atom ($\sim 87\%$) which is doubly occupied in all the studied electronic states. The 2σ bonding molecular orbital is a result of the hybridization of the atomic orbitals $6s(\text{Hf})$, $5d_{z^2}(\text{Hf})$, with a larger contribution from the $2p_z(\text{N})$. Specifically, the % contributions of the aforementioned atomic orbitals on the 2σ are approximately 17%, 18%, and 64%, respectively. The 3σ is predominantly the $6s(\text{Hf})$ ($\sim 72\%$) with a minor fraction of $5d_{z^2}(\text{Hf})$ ($\sim 15\%$). The hybridization of the $5d_{yz}(\text{Hf}) + 2p_y(\text{N})$ and $5d_{xz}(\text{Hf}) + 2p_x(\text{N})$ produces the $1\pi_y$ and $1\pi_x$ bonding molecular orbitals, respectively. On the other hand, the $5d_{yz}(\text{Hf}) - 2p_y(\text{N}) - 6p_y(\text{Hf})$ and $5d_{xz}(\text{Hf}) - 2p_x(\text{N}) - 6p_x(\text{Hf})$ give rise to the $2\pi_y$ and $2\pi_x$ orbitals, respectively. See ESI,[†] Table S1 for % atomic orbitals contribution on these molecular orbitals. The $1\delta_{x^2-y^2}$ and $1\delta_{xy}$ orbitals do not mix with the

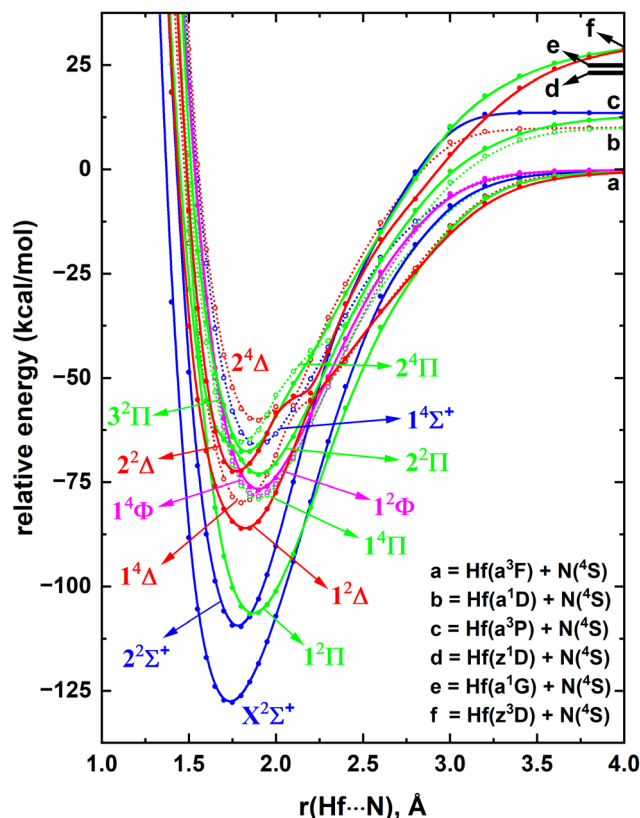


Fig. 1 Full MRCI PECs of HfN as a function of Hf...N distance $[r(\text{Hf}\cdots\text{N}), \text{\AA}]$. The relative energies are referenced to the total energy of the $\text{Hf}(a^3F) + \text{N}(^4S)$ fragments at $r = 12\text{ \AA}$, which is set to 0 kcal mol^{-1} . The Σ^+ , Π , Δ , and Φ states are shown in blue, green, red, and pink colors, respectively. The solid and dotted PECs represent doublet and quartet spins, respectively.

atomic orbitals of N atoms and are purely the $5d_{x^2-y^2}$ and $5d_{xy}$ atomic orbitals of Hf.

The ground state of the HfN has the $1\sigma^22\sigma^23\sigma^11\pi^4$ electron configuration. Based on this electron arrangement and the contours of the occupying molecular orbitals, we can expect triple-bonded nature for the ground state of HfN. The promotion of an electron from the 2σ to 3σ produces its first excited electronic state ($2^2\Sigma^+$). On the other hand, moving an electron from $1\pi_x$ to 3σ from the $X^2\Sigma^+$ gives rise to the $1^2\Pi$ state of HfN. The destabilization of the $2^2\Sigma^+$ and $1^2\Pi$ compared to the $X^2\Sigma^+$ is expected due to the replacement of an electron from a bonding orbital of $X^2\Sigma^+$ (2σ or $1\pi_x$) to a non-bonding 3σ orbital. Note that all three of these electronic states of HfN are single-reference in nature and the proceeding $1^2\Delta$ is the lowest energy multireference state of HfN. Furthermore, this is the first electronic state of HfN that carries populated δ orbitals (Table 1). The $1^2\Delta$ is followed by the first quartet-spin electronic state of HfN ($1^4\Delta$) which also possesses an electron in δ orbitals. The $1^4\Delta$ is a single-reference state and all the proceeding electronic states except for $2^4\Pi$ are multireference in nature (Table 1). Based on the dominant electron configurations and the shapes of the occupying molecular orbitals, the valence-bond-Lewis (vBL) diagrams were proposed for the first five electronic states of HfN (Fig. 3).

Table 1 Dominant electronic configurations at equilibrium distances of the studied fourteen electronic states of HfN

State ^a	Coefficient ^b	Configuration ^c
$X^2\Sigma^+$	0.93	$1\sigma^2 2\sigma^2 3\sigma 1\pi_x^2 1\pi_y^2$
$2^2\Sigma^+$	0.93	$1\sigma^2 2\sigma 3\sigma^2 1\pi_x^2 1\pi_y^2$
$1^2\Pi$ (B_1)	0.91	$1\sigma^2 2\sigma^2 3\sigma^2 1\pi_x 1\pi_y^2$
$1^2\Delta$ (A_2)	0.69 −0.49 0.31	$1\sigma^2 2\sigma^2 1\pi_x^2 1\pi_y^2 1\delta_{xy}$ $1\sigma^2 2\sigma 3\sigma 1\pi_x^2 1\pi_y^2 1\delta_{xy}$ $1\sigma^2 2\sigma 3\sigma 1\pi_x^2 1\pi_y^2 1\delta_{xy}$
$1^4\Delta$ (A_1)	0.95	$1\sigma^2 2\sigma 3\sigma 1\pi_x^2 1\pi_y^2 (1\delta_{x^2-y^2})$
$1^4\Pi$ (B_1)	−0.66 0.66	$1\sigma^2 2\sigma^2 3\sigma 1\pi_x 1\pi_y^2 (1\delta_{x^2-y^2})$ $1\sigma^2 2\sigma^2 3\sigma 1\pi_x^2 1\pi_y 1\delta_{xy}$
$1^4\Phi$ (B_1)	0.67 0.67	$1\sigma^2 2\sigma^2 3\sigma 1\pi_x 1\pi_y^2 (1\delta_{x^2-y^2})$ $1\sigma^2 2\sigma^2 3\sigma 1\pi_x^2 1\pi_y 1\delta_{xy}$
$1^2\Phi$ (B_1)	0.54 0.54	$1\sigma^2 2\sigma^2 3\sigma 1\pi_x 1\pi_y^2 (1\delta_{x^2-y^2})$ $1\sigma^2 2\sigma^2 3\sigma 1\pi_x^2 1\pi_y 1\delta_{xy}$
$2^2\Pi$ (B_1)	0.53 −0.53	$1\sigma^2 2\sigma^2 3\sigma 1\pi_x 1\pi_y^2 (1\delta_{x^2-y^2})$ $1\sigma^2 2\sigma^2 3\sigma 1\pi_x^2 1\pi_y 1\delta_{xy}$
$2^2\Delta$ (A_1)	−0.42 0.60 −0.54	$1\sigma^2 2\sigma^2 1\pi_x^2 1\pi_y^2 (1\delta_{x^2-y^2})$ $1\sigma^2 2\sigma 3\sigma 1\pi_x^2 1\pi_y^2 (1\delta_{x^2-y^2})$ $1\sigma^2 2\sigma 3\sigma 1\pi_x^2 1\pi_y^2 (1\delta_{x^2-y^2})$
$3^2\Pi$ (B_1)	0.60 −0.53 0.31	$1\sigma^2 2\sigma^2 1\pi_x^2 2\pi_x 1\pi_y^2$ $1\sigma^2 2\sigma 3\sigma 1\pi_x^2 2\pi_x 1\pi_y^2$ $1\sigma^2 2\sigma 3\sigma 1\pi_x^2 2\pi_x 1\pi_y^2$
$1^4\Sigma^+$	0.64 0.64	$1\sigma^2 2\sigma^2 3\sigma 1\pi_x 2\pi_x 1\pi_y^2$ $1\sigma^2 2\sigma^2 3\sigma 1\pi_x^2 1\pi_y 2\pi_y$
$2^4\Pi$ (B_1)	0.93	$1\sigma^2 2\sigma 3\sigma 1\pi_x^2 2\pi_x 1\pi_y^2$
$2^4\Delta$ (A_2)	0.63 −0.63	$1\sigma^2 2\sigma^2 3\sigma 1\pi_x^2 2\pi_x 1\pi_y$ $1\sigma^2 2\sigma^2 3\sigma 1\pi_x 1\pi_y^2 2\pi_y$

^a Only one component under C_{2v} symmetry is listed for Π , Δ , and Φ states. The respective irreducible representations are provided in parentheses. ^b All the configuration interaction coefficients that are larger than 0.30 of the corresponding natural orbital representations are listed. ^c β and α -spin electrons are specified with and without bars over the spatial orbital, respectively.

The spin-orbit effects of the heavier third-row TM species are significant. Hence, we have investigated the spin-orbit effects of a few low-lying electronic states of HfN at the MRCI level. Here, to construct the spin-orbit matrix, the $X^2\Sigma^+$, $2^2\Sigma^+$, $1^2\Pi$, and $1^2\Delta$ states were used. The spin-orbit coupling produces the $\Omega = 1/2$ ($X^2\Sigma^+$), $\Omega = 1/2$ ($2^2\Sigma^+$), $\Omega = 3/2$ and $1/2$ ($1^2\Pi$), $\Omega = 5/2$ and $3/2$ ($1^2\Delta$) components. The MRCI spin-orbit PECs with respect to the Hf–N distance are given in Fig. 4. The $\Omega = 1/2$ ground state spin-orbit curve is mildly affected by the high-lying $\Omega = 1/2$ states. The excited $\Omega = 1/2$ components of each $2^2\Sigma^+$ and $1^2\Pi$ show an avoided crossing around the 1.85 Å. Similarly, the $\Omega = 3/2$ products of the $1^2\Pi$ and $1^2\Delta$ undergo an avoided crossing at ~1.6 Å. Overall, among the studied states, the ordering of the Ω states of HfN are 1/2, 1/2, 3/2, 1/2, 3/2, 5/2 (Fig. 4). More information on the spin-orbit effects on the

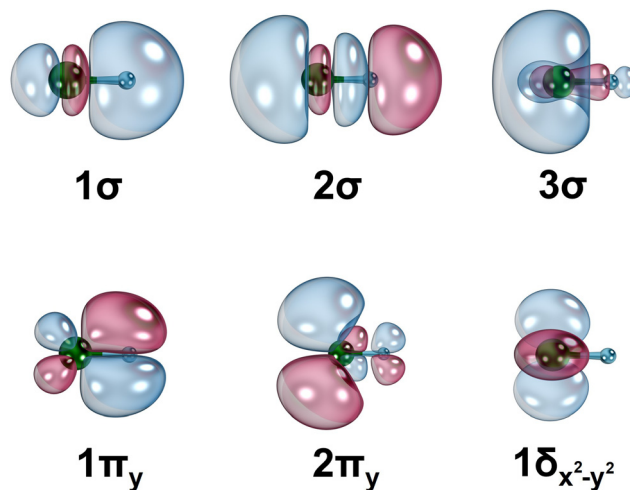


Fig. 2 Select CASSCF state average molecular orbitals of HfN. The Hf and N atoms are depicted in green and blue, respectively. The 90° rotation of $1\pi_y$ and $2\pi_y$ orbitals along the principal axis yields $1\pi_x$ and $2\pi_x$ orbitals, respectively, whereas the 45° rotation of $1\delta_{x^2-y^2}$ produces $1\delta_{xy}$ orbital. The contours were produced using the IboView software.⁴⁷ The molecular orbitals of HfN⁺ have similar shapes.

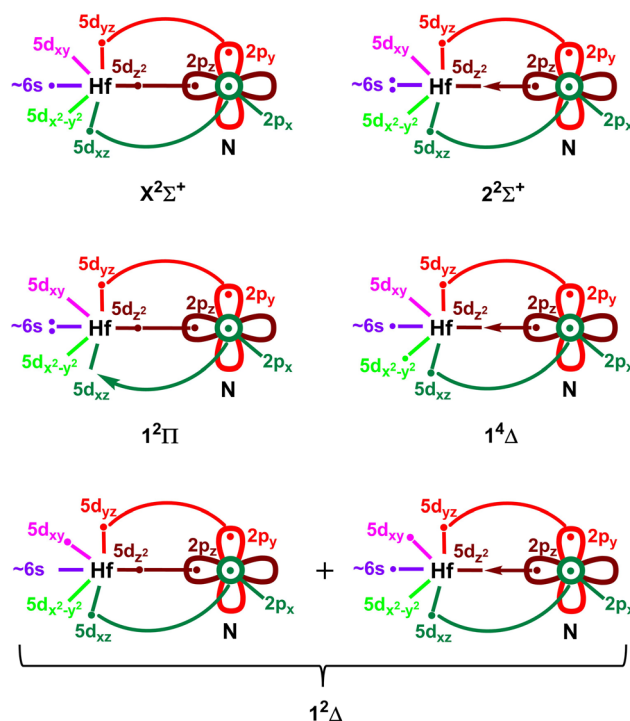


Fig. 3 Proposed vbL diagrams for the five lowest energy electronic states of HfN. In all cases, the 2s orbital of nitrogen is doubly occupied and not shown for clarity. The dominant configuration of the $1^2\Delta$ state is shown in the bottom-left vbL diagram, whereas its two minor components that bear similar electron arrangements are shown in the bottom-right diagram. See Table 1 for their exact electronic configurations.

ground and excited states of HfN are given in Table 2, ESI,[†] Table S2, and in the upcoming paragraphs of the paper.



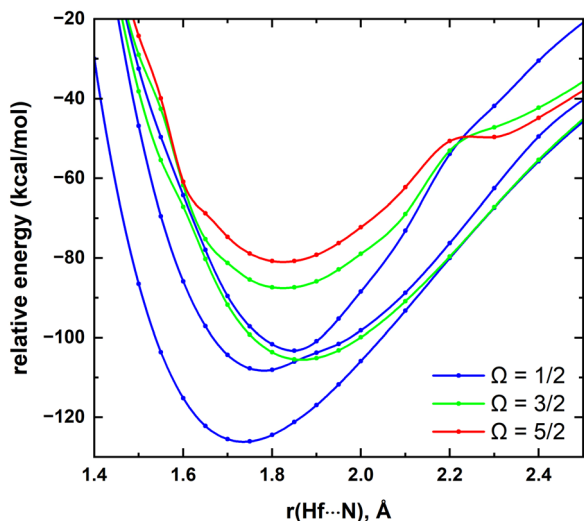


Fig. 4 MRCI spin-orbit coupling curves resulting from $X^2\Sigma^+$, $2^2\Sigma^+$, $1^2\Pi$, and $1^2\Delta$ electronic states of HfN as a function of Hf...N distance $[r(\text{Hf}\cdots\text{N}), \text{\AA}]$. The relative energies are referenced to the lowest energy spin-orbit curve at $r = 12 \text{ \AA}$, which is set to 0 kcal mol^{-1} . The $\Omega = 1/2$, $\Omega = 3/2$, and $\Omega = 5/2$ curves are shown in blue, green, and red, respectively. See Fig. 1 for the PECs of their parent $X^2\Sigma^+$, $2^2\Sigma^+$, $1^2\Pi$, and $1^2\Delta$ states.

We have exploited several single-reference electronic states of HfN to perform CCSD(T) calculations. Furthermore, due to the relatively less expensive nature of CCSD(T) compared to MRCI, at the CCSD(T) level core electron correlation effects and the basis set effects were tested. The calculated multireference and coupled cluster results of the HfN are listed in Table 2. The D_e of HfN($X^2\Sigma^+$) is $127.90 \text{ kcal mol}^{-1}$ at the MRCI level, which is $3.2 \text{ kcal mol}^{-1}$ lower compared to the MRCI+Q D_e (Table 2). Our MRCI D_e is only slightly lower compared to the CBS-CCSD(T) D_0 reported by Merriles *et al.*, (*i.e.*, $127.99 \text{ kcal mol}^{-1}$).³⁰ The CCSD(T) D_e of the HfN($X^2\Sigma^+$) calculated in the present work with the aug-cc-pVQZ(N) cc-pVQZ-PP(Hf) basis set is nearly identical to the MRCI+Q value (130.88 versus $131.06 \text{ kcal mol}^{-1}$). The $5s^25p^6$ core electrons of Hf correlation [*i.e.*, QZ-C-CCSD(T)] increased the D_e of the HfN($X^2\Sigma^+$) by $1.81 \text{ kcal mol}^{-1}$. Moving to the larger aug-cc-pV5Z(N) cc-pwCV5Z-PP(Hf) basis set [*i.e.*, 5Z-C-CCSD(T)] further increased the D_e of HfN($X^2\Sigma^+$), which is a common observation in the literature.^{7,46} The CBS-C-CCSD(T) only increased the D_e by $0.92 \text{ kcal mol}^{-1}$ compared to the 5Z-C-CCSD(T) D_e . The zero-point energy corrected CBS-C-CCSD(T) D_0 is $133.94 \text{ kcal mol}^{-1}$ which is almost identical to the upper limit of the D_0 reported by the Kohl and Stearns in 1973 [*i.e.*, $126.83(7.15) \text{ kcal mol}^{-1}$].²⁵ The experimental D_0 value reported by Merriles *et al.*, for the HfN($X^2\Sigma^+$) [*i.e.*, $5.374(4) \text{ eV}$ or $\sim 124 \text{ kcal mol}^{-1}$] is $\sim 4 \text{ kcal mol}^{-1}$ lower than the smallest D_e ($127.90 \text{ kcal mol}^{-1}$ at MRCI) reported in this work (Table 2).³⁰ The inclusion of spin-orbit effects at the MRCI level decreased our D_e of HfN ($X^2\Sigma^+_{1/2}$) to $126.17 \text{ kcal mol}^{-1}$. Furthermore, with the inclusion of zero-point energy, this value dropped further to $124.86 \text{ kcal mol}^{-1}$ (D_0), which is in perfect harmony with the Merriles *et al.*'s value. A better agreement between CCSD(T) versus MRCI+Q was also observed for the D_e of $1^2\Pi$ and $1^4\Delta$.

Similar to the ground state, these CCSD(T) values are slightly smaller compared to the MRCI+Q values. The increment of D_e moving from CCSD(T) to QZ-C-CCSD(T) and QZ-C-CCSD(T) to 5Z-C-CCSD(T) was also observed for the $1^2\Pi$ state. Overall, for all fourteen states the MRCI+Q D_e are $1.7\text{--}3.3 \text{ kcal mol}^{-1}$ higher compared to the MRCI D_e .

For all the states, the MRCI+Q predicted r_e values are slightly longer compared to the MRCI r_e (by $0.001\text{--}0.006 \text{ \AA}$). Similarly, the MRCI+Q r_e values are longer than the coupled cluster r_e values (Table 2). According to the available QZ-C-CCSD(T) and CCSD(T) results, the core electron correlation tends to shorten the bond distance (by $\sim 0.02 \text{ \AA}$), which we have seen in our earlier studies.^{48,49} The r_e of the spin-orbit ground state $X^2\Sigma^+_{1/2}$ is identical to the spin-orbit effect neglected MRCI value of the ground state (*i.e.*, 1.736 \AA). Since the spin-orbit effects are insignificant for the r_e of the $X^2\Sigma^+$, a direct comparison between coupled cluster versus experiment can be made. Our coupled cluster r_e values under QZ-C-CCSD(T), 5Z-C-CCSD(T), and CBS-C-CCSD(T) for the $X^2\Sigma^+$ are 1.718 , 1.715 , and 1.714 \AA , respectively which align well with the experimental r_e reported by Ram and Bernath which is $1.724678(36) \text{ \AA}$.²⁷ Furthermore, upon comparison with the literature theoretical analysis, the DFT/BP86 r_e reported by Kushto *et al.*,²⁸ (*i.e.*, 1.734 \AA) for the ground state is in harmony with our MRCI and CCSD(T) value, whereas the DFT/B3LYP r_e by Hong *et al.*,²⁹ (1.764 \AA) is longer compared to all the r_e values reported in the present work (Table 2).

The first excitation energy with the spin-orbit effects is 6264 cm^{-1} which is only 79 cm^{-1} lower compared to the spin-orbit untreated excitation energy (Table 2). The 0-0 band of the $[6.7]^2\Sigma^+-X^2\Sigma^+$ transition of the HfN reported by Ram and Bernath is 6668 cm^{-1} which is 404 cm^{-1} higher than our spin-orbit treated first excitation energy of HfN.²⁷ Upon comparison of spin-orbit untreated MRCI+Q T_e with MRCI T_e values, the MRCI+Q T_e values are higher (by $155\text{--}510 \text{ cm}^{-1}$) compared to the MRCI except for the $2^2\Delta$ state that predicted 36 cm^{-1} lower T_e by MRCI+Q compared to the MRCI value.

The experimental ω_e and $\omega_e x_e$ values reported by Ram and Bernath for the $X^2\Sigma^+$ are $932.7164(15) \text{ cm}^{-1}$ and $4.41299(65) \text{ cm}^{-1}$, respectively.²⁷ The CCSD(T) predicted the closest ω_e value (*i.e.*, 937 cm^{-1}) to their finding by underestimating the $\omega_e x_e$ by $\sim 0.4 \text{ cm}^{-1}$ (Table 2). However, the CBS extrapolation increases the ω_e value to 961 cm^{-1} , while decreasing the $\omega_e x_e$ to 3.4 cm^{-1} . Interestingly, the CCSD(T) ω_e and $\omega_e x_e$ values are in better agreement with the values of Ram and Bernath compared to our spin-orbit treated MRCI ω_e (916 cm^{-1}) and $\omega_e x_e$ (4.9 cm^{-1}) values of the ground state $X^2\Sigma^+_{1/2}$ (Table 2).

The μ values can be used to predict spectra, opacities, and radiative properties of molecular species and hence are often calculated using *ab initio* techniques.^{50–53} The MRCI DMCs of the first five electronic states of HfN are given in Fig. 5. The μ of HfN($X^2\Sigma^+$) calculated under the DFT/B3LYP with aug-cc-pVQZ(N) aug-cc-pVQZ-PP(Hf) basis set by Merriles *et al.*, is 5.50 D .³⁰ This value is in reasonable agreement with the μ of HfN($X^2\Sigma^+$) obtained at the finite-field approach with CCSD(T) (*i.e.*, -5.37 D). Since Hf is placed to the left of the coordinate point zero of the z -axis in our calculations, the negative μ value



Table 2 Dissociation energy with respect to ground state fragments (D_e , kcal mol⁻¹), bond length (r_e , Å), excitation energy (T_e , cm⁻¹), harmonic vibrational frequency (ω_e , cm⁻¹), and anharmonicity ($\omega_e x_e$, cm⁻¹) of low-lying states of HfN

State	Method ^a	D_e	r_e	T_e	ω_e	$\omega_e x_e$
$X^2\Sigma^+$	MRCI	127.90	1.736	—	924	4.9
	MRCI-SOC ($\Omega = 1/2$)	126.17	1.736	—	916	4.9
	MRCI+Q	131.06	1.739	—	915	4.7
	CCSD(T)	130.88	1.735	—	937	4.0
	QZ-C-CCSD(T)	132.69	1.718	—	953	3.6
	5Z-C-CCSD(T)	134.39	1.715	—	958	3.5
	CBS-C-CCSD(T)	135.31	1.714	—	961	3.4
	CBS-CCSD(T) ³⁰	$D_0 = 127.99$	—	—	—	—
	DFT/BP86 ²⁸	—	1.734	—	942	—
	DFT/B3LYP ²⁹	113.92	1.764	—	940	—
	Experiment	$D_0 = 123.93(9)^{30}$ $D_0 = 141^{24}$ $D_0 = 126.83(7.15)^{25}$	1.69(30) ²⁶ 1.724678(36) ²⁷	—	919.5(20) ²⁶ 932.7164(15) ²⁷	4.41299(65) ²⁷
$2^2\Sigma^{+b}$	MRCI	109.77	1.780	6343	993	5.0
	MRCI-SOC ($\Omega = 1/2$)	108.26	1.781	6264	862	18.4
	MRCI+Q	112.48	1.786	6498	981	4.8
$1^2\Pi$	MRCI	106.70	1.867	7417	927	5.4
	MRCI-SOC ($\Omega = 3/2$)	105.54	1.866	7216	939	12.6
	MRCI-SOC ($\Omega = 1/2$)	103.25	1.847	8015	1095	7.9
	MRCI+Q	108.61	1.871	7851	927	3.7
	CCSD(T)	107.55	1.867	8161	835	3.3
	QZ-C-CCSD(T)	108.56	1.846	8439	848	3.2
	5Z-C-CCSD(T)	109.64	1.844	8657	851	3.4
$1^2\Delta$	MRCI	86.25	1.822	14 567	768	4.8
	MRCI-SOC ($\Omega = 3/2$)	87.58	1.825	13 498	795	1.9
	MRCI-SOC ($\Omega = 5/2$)	81.01	1.825	15 796	797	2.0
	MRCI+Q	88.90	1.823	14 744	736	6.1
$1^4\Delta$	MRCI	79.93	1.806	16 777	873	4.3
	MRCI+Q	82.50	1.810	16 982	873	5.5
	CCSD(T)	82.27	1.809	17 002	869	3.2
$1^4\Pi$	MRCI	78.97	1.895	17 113	750	4.0
	MRCI+Q	80.94	1.896	17 528	750	4.3
$1^4\Phi$	MRCI	78.31	1.896	17 345	749	4.0
	MRCI+Q	80.27	1.897	17 765	749	4.1
$1^2\Phi$	MRCI	76.82	1.898	17 865	759	3.9
	MRCI+Q	78.95	1.900	18 226	758	4.0
$2^2\Pi$	MRCI	73.25	1.898	19 116	800	22.6
	MRCI+Q	75.55	1.900	19 415	840	24.7
$2^2\Delta$	MRCI	72.82	1.772	19 267	856	8.5
	MRCI+Q	76.07	1.777	19 231	856	9.6
$3^2\Pi$	MRCI	67.94	1.824	20 972	881	9.2
	MRCI+Q	70.60	1.826	21 147	889	8.2
$1^4\Sigma^+$	MRCI	66.24	1.894	21 565	753	7.3
	MRCI+Q	67.94	1.899	22 075	733	6.1
$2^4\Pi$	MRCI	65.45	1.809	21 842	887	11.6
	MRCI+Q	67.79	1.814	22 128	864	11.5
$2^4\Delta$	MRCI	60.14	1.888	23 700	724	46.8
	MRCI+Q	61.91	1.892	24 187	682	39.7

^a Davidson corrected MRCI is denoted by MRCI+Q. For all MRCI, MRCI+Q, and CCSD(T) calculations cc-pVQZ-PP (60ECP) of Hf and aug-cc-pVQZ of N basis set was applied. The 5s²5p⁶ (of Hf) core electrons correlated CCSD(T) calculations are labeled as XZ-C-CCSD(T) and the appropriate weighted-core cc-pwCVXZ-PP (60ECP) basis set of Hf was used (X = Q, 5). The MRCI findings of Ω states of the four lowest electronic states of HfN are listed in the MRCI-SOC rows. ^b CCSD(T) results of the single-reference $2^2\Sigma^+$ state are not included due to convergence issues.

implies that the μ vector points to Hf. Under the same CCSD(T) are identical (*i.e.*, -5.35 D). Similarly, the CCSD(T) μ approach, μ values calculated at the QZ-C-CCSD(T) and 5Z-C- values of single-reference $1^2\Pi$ and $1^4\Delta$ were also calculated and



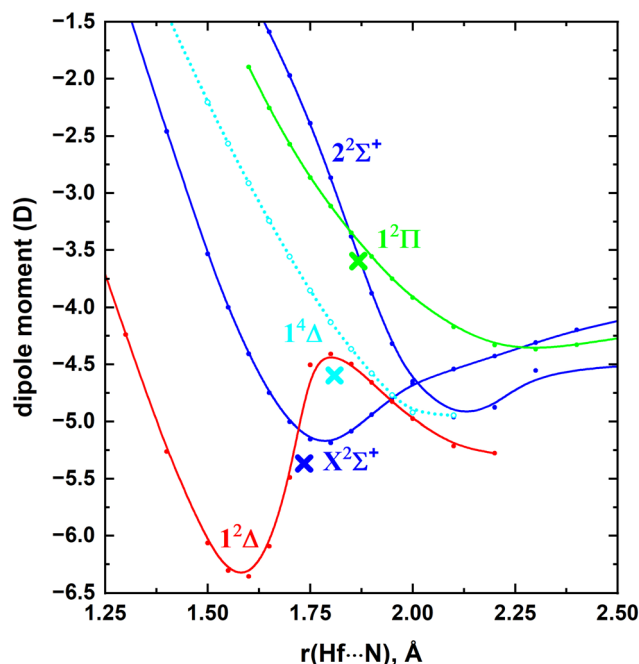


Fig. 5 MRCI DMCs of the lowest five electronic states of HfN⁺ as a function of Hf...N distance [$r(\text{Hf}\cdots\text{N})$, Å]. The CCSD(T) μ values of $X^2\Sigma^+$, $1^2\Pi$, and $1^4\Delta$ calculated at their equilibrium bond distances are depicted in blue (at -5.37 D), green (at -3.59 D), and cyan (at -4.60 D) cross marks, respectively.

are -3.59 and -4.60 D, respectively. The MRCI μ values calculated at the equilibrium bond distances for these electronic states deviate from the CCSD(T) by 0.2 – 0.5 D (Fig. 5).

III.B. HfN⁺

The removal of an electron from the $5d$ shell of the ground state of Hf(a^3F ; $5d^26s^2$) yields the ground state of Hf⁺(a^2D ; $5d^16s^2$).⁴⁴ The experimental IE of this process is 6.82507 eV.⁵⁴ Under the implemented CCSD(T), QZ-C-CCSD(T), 5Z-C-CCSD(T), and CBS-C-CCSD(T) levels in this work, the IE of Hf is 6.531 , 6.735 , 6.757 , and 6.762 eV respectively. Notice that the discrepancy between the CCSD(T) IE *versus* experimental IE is 0.294 eV, whereas it is 0.09 eV between QZ-C-CCSD(T) *versus* experiment. This displays the importance of the core electron correlation on gaining more accurate IE values. Indeed, as expected the more expensive 5Z-C-CCSD(T) and CBS-C-CCSD(T) predicted IE values are in better agreement with the experiment. The first excited state of Hf⁺(a^4F) lies ~ 10 – 24 kcal mol^{−1} above the ground state and carries the $5d^26s^1$ valence electron configuration.⁴⁴ Similarly, the next five excited states of Hf⁺ (*i.e.*, a^4P , a^2F , b^2D , a^2P , a^2G) that span between ~ 34 – 51 kcal mol^{−1} have $5d^26s^1$ configuration.⁴⁴ The seventh excited state of Hf⁺(b^4F) is the first state of Hf⁺ with a vacant $6s$ orbital which carries three electrons in the $5d$ shell (~ 54 – 67 kcal mol^{−1}).⁴⁴

The first IE of the N atom (*i.e.*, 14.5341 eV) is more than twice high compared to that of Hf.⁵⁴ Hence, in this work, the reactions between the low-lying electronic states of Hf⁺ *versus* the ground state of N(4S) were selected to study the PECs of HfN⁺. Specifically, all the PECs arising from the Hf⁺(a^2D) +

N(4S), Hf⁺(a^4F) + N(4S), and Hf⁺(a^4P) + N(4S) fragments and the singlet-spin molecular states generating from Hf⁺(b^4F) + N(4S) were studied. The first three combinations give rise to 5(quintet + triplet), 7(septet + quintet + triplet + singlet), and 3(septet + quintet + triplet + singlet) states. The union of high energy Hf⁺(b^4F) + N(4S) gives out 7(septet + quintet + triplet + singlet) states but in our CASSCF calculations only the seven singlet-spin PECs of this channel were included. Of course, we expect a series of quintet- and triplet-spin electronic states to be produced from the Hf⁺(a^2F) + N(4S), Hf⁺(b^2D) + N(4S), Hf⁺(a^2P) + N(4S), and Hf⁺(a^2G) + N(4S) fragments. However, according to our preliminary analysis these quintet- and triplet-spin states are not among the most stable states of HfN⁺. However, the high energy Hf⁺(b^4F) + N(4S) produces a reasonably stable singlet-spin states and hence here they were studied. Overall, at the CASSCF level 57 states were studied and the lowest eighteen electronic states of HfN⁺ were identified to investigate under the MRCI level. The MRCI PECs HfN⁺ are given in Fig. 6.

The ground state of the HfN⁺ is a $X^1\Sigma^+$ with an equilibrium distance of ~ 1.7 Å (Fig. 6). It is originating from the second lowest energy fragments [*i.e.*, Hf⁺(a^4F) + N(4S)] and lies well separated from its first excited state (*i.e.*, $1^3\Sigma^+$). Similar to $X^1\Sigma^+$, $1^3\Sigma^+$ dissociates to Hf⁺(a^4F) + N(4S). The second excited state of HfN⁺($2^1\Sigma^+$) is very close in energy to the $1^3\Sigma^+$ (energy difference is less than 2 kcal mol^{−1}) and is originating from Hf⁺(a^4P) + N(4S). This state is followed by several Π , Δ , Φ , and Σ^- electronic states and the spectrum becomes rather complicated around the 35 – 50 kcal mol^{−1} region (Fig. 6). Furthermore, in this region we see avoided crossings between the $1^3\Delta$ *versus* $2^3\Delta$ and $1^4\Delta$ *versus* $2^4\Delta$ PECs.

The ground state of HfN⁺($X^1\Sigma^+$) can be created by detaching an electron from the 3σ orbital of the HfN($X^2\Sigma^+$) (compare the electronic configurations listed in Tables 1 and 3). This process requires 7.207 eV at the CCSD(T). At the QZ-C-CCSD(T), 5Z-C-CCSD(T), and CBS-C-CCSD(T) levels they are 7.408 , 7.405 eV, and 7.401 respectively. Excitation of an electron from the HfN⁺($X^1\Sigma^+$) 2σ to 3σ creates the electron configuration of the first excited state of HfN⁺ (*i.e.*, $1^3\Sigma^+$). Both $X^1\Sigma^+$ and $1^3\Sigma^+$ states are dominantly single-reference in nature. The next state of HfN⁺ (*i.e.*, $2^1\Sigma^+$) is the corresponding multireference open-shell singlet of the $1^3\Sigma^+$ state. Notice that an ionization of a 3σ electron from the HfN($2^2\Sigma^+$) gives rise to $1^3\Sigma^+$ and $2^1\Sigma^+$ states of HfN⁺. By a similar electron ionization from the HfN($1^2\Pi$), the third and fourth excited states of HfN⁺ ($1^3\Pi$ and $1^1\Pi$) can be created. The next state of HfN⁺ is a single-reference $1^3\Delta$ which is followed by a series of multireference states (*i.e.*, $1^1\Delta$, $1^3\Phi$, $1^1\Phi$, $2^3\Pi$, $2^1\Pi$, $1^3\Sigma^-$). The first quintet-spin electronic state of HfN⁺ (*i.e.*, $1^5\Delta$) falls just above the $1^3\Sigma^-$. The proposed vBL diagrams based on the electron arrangements of the seven most stable electronic states of HfN⁺ are given in Fig. 7.

In this work, the low-lying $X^1\Sigma^+$, $1^3\Sigma^+$, $2^1\Sigma^+$, $1^3\Pi$, $1^1\Pi$ electronic states of HfN⁺ were used to construct a spin-orbit matrix and study their corresponding spin-orbit components. The spin-orbit coupling produces the $\Omega = 0^+$ ($X^1\Sigma^+$), $\Omega = 0^-$ and 1 ($1^3\Sigma^+$), $\Omega = 0^+$ ($2^1\Sigma^+$), $\Omega = 2, 1, 0^+$, and 0^- ($1^3\Pi$), and $\Omega = 1$ ($1^1\Pi$) products and they are depicted in Fig. 8. The energy difference



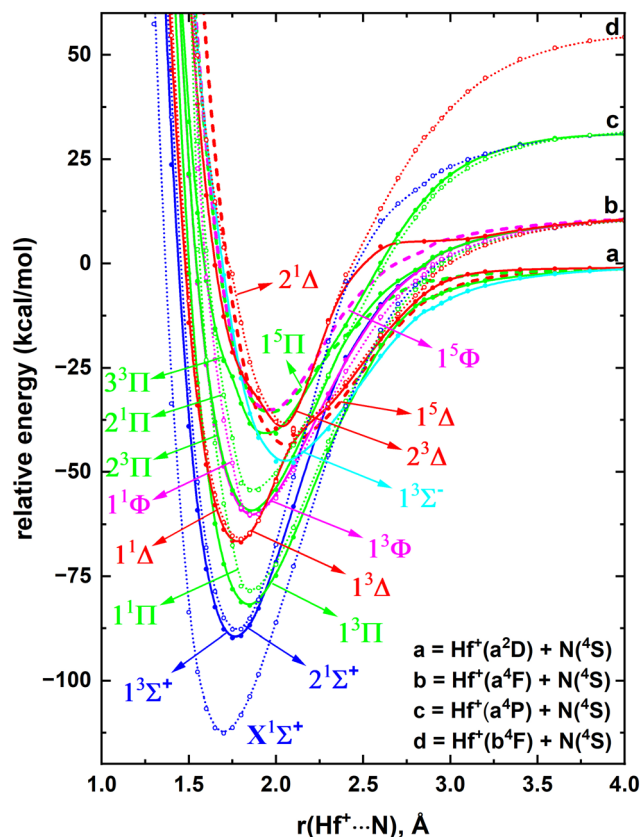


Fig. 6 Full MRCI PECs of HfN^+ as a function of $\text{Hf}^+\cdots\text{N}$ distance [$r(\text{Hf}^+\cdots\text{N})$, Å]. The relative energies are referenced to the total energy of the $\text{Hf}^+(\text{a}^2\text{D}) + \text{N}(\text{^4S})$ at $r = 12$ Å, which is set to 0 kcal mol $^{-1}$. The Σ^+ , Π , Δ , Φ , and Σ^- states are shown in blue, green, red, pink, and cyan, respectively. The solid, dotted, and dashed PECs represent triplet, singlet, and quintet spins, respectively.

between the $\Omega = 0^-$ and 1 components of $1^3\Sigma^+$ are minor and similarly the $\Omega = 2, 1, 0^+$, and 0^- products of the $1^3\Pi$ are also energetically closely arranged. The spectroscopic constants and compositions of the spin-orbit states are listed in Table 4 and ESI, † Table S4.

Under the utilized methods, the D_e of $\text{HfN}^+(\text{X}^1\Sigma^+)$ varied between 112–121 kcal mol $^{-1}$ (Table 4). Specifically, the highest level of coupled cluster approach, CBS-C-CCSD(T), predicted the largest D_e (i.e., 120.56 kcal mol $^{-1}$). These D_e values calculated in the present work are significantly higher than the previously reported DFT/B3LYP value by Hong *et al.* (i.e., 91.55 kcal mol $^{-1}$). 29 The spin-orbit corrected MRCI D_e of $\text{HfN}^+(\text{X}^1\Sigma^+)$ is 110.48 kcal mol $^{-1}$. The zero-point energy correction decreases the D_0 of $\text{HfN}^+(\text{X}^1\Sigma^+)$ to 109.10 kcal mol $^{-1}$. Compared to the D_e of the $\text{HfN}(\text{X}^2\Sigma^+)$, the D_e of $\text{HfN}^+(\text{X}^1\Sigma^+)$ is ~ 15 kcal mol $^{-1}$ lower under all levels of theory (Table 2 and Table 4). Similar to HfN , the D_e increased in the order of CCSD(T) < QZ-C-CCSD(T) < 5Z-C-CCSD(T) for HfN^+ (see the D_e of $\text{X}^1\Sigma^+$, $1^3\Sigma^+$, $1^3\Pi$, and $1^3\Delta$ in Table 4). Furthermore, for all the states, the MRCI predicted D_e are slightly smaller (by 1.1–3.3 kcal mol $^{-1}$) compared to the MRCI+Q values, which is a consistent observation with the D_e of HfN .

Due to the electrostatic attraction between Hf^+ and N, we can expect a shorter r_e value for HfN^+ compared to HfN . Indeed, this

Table 3 Dominant electronic configurations at equilibrium distances of the studied eighteen electronic states of HfN^+

State ^a	Coefficient ^b	Configuration ^c
$\text{X}^1\Sigma^+$	0.95	$1\sigma^2 2\sigma^2 1\pi_x^2 1\pi_y^2$
$1^3\Sigma^+$	0.91	$1\sigma^2 2\sigma 3\sigma 1\pi_x^2 1\pi_y^2$
$2^1\Sigma^+$	−0.65	$1\sigma^2 \bar{2}\sigma 3\sigma 1\pi_x^2 1\pi_y^2$
	0.65	$1\sigma^2 2\sigma 3\sigma 1\pi_x^2 1\pi_y^2$
$1^3\Pi$ (B_1)	0.88	$1\sigma^2 2\sigma^2 3\sigma 1\pi_x 1\pi_y^2$
$1^1\Pi$ (B_1)	0.63	$1\sigma^2 2\sigma^2 \bar{3}\sigma 1\pi_x 1\pi_y^2$
	−0.63	$1\sigma^2 2\sigma^2 3\sigma 1\pi_x 1\pi_y^2$
$1^3\Delta$ (A_2)	0.92	$1\sigma^2 2\sigma 1\pi_x^2 1\pi_y^2 1\delta_{xy}$
$1^1\Delta$ (A_2)	0.65	$1\sigma^2 2\sigma 1\pi_x^2 1\pi_y^2 \bar{1}\delta_{xy}$
	−0.65	$1\sigma^2 \bar{2}\sigma 1\pi_x^2 1\pi_y^2 1\delta_{xy}$
$1^3\Phi$ (B_1)	0.65	$1\sigma^2 2\sigma^2 1\pi_x 1\pi_y^2 (1\delta_{x^2-y^2})$
	0.65	$1\sigma^2 2\sigma^2 1\pi_x 1\pi_y 1\delta_{xy}$
$1^1\Phi$ (B_1)	−0.45	$1\sigma^2 2\sigma^2 1\pi_x^2 1\pi_y \bar{1}\delta_{xy}$
	0.45	$1\sigma^2 2\sigma^2 1\pi_x^2 1\pi_y 1\delta_{xy}$
	0.45	$1\sigma^2 2\sigma^2 1\pi_x 1\pi_y^2 (1\delta_{x^2-y^2})$
	−0.45	$1\sigma^2 2\sigma^2 \bar{1}\pi_x 1\pi_y^2 (1\delta_{x^2-y^2})$
$2^3\Pi$ (B_1)	−0.62	$1\sigma^2 2\sigma^2 1\pi_x 1\pi_y^2 (1\delta_{x^2-y^2})$
	0.62	$1\sigma^2 2\sigma^2 1\pi_x 1\pi_y 1\delta_{xy}$
$2^1\Pi$ (B_1)	−0.46	$1\sigma^2 2\sigma^2 1\pi_x^2 1\pi_y \bar{1}\delta_{xy}$
	0.46	$1\sigma^2 2\sigma^2 1\pi_x^2 1\pi_y 1\delta_{xy}$
	0.46	$1\sigma^2 2\sigma^2 1\pi_x 1\pi_y^2 (1\delta_{x^2-y^2})$
	−0.46	$1\sigma^2 2\sigma^2 \bar{1}\pi_x 1\pi_y^2 (1\delta_{x^2-y^2})$
$1^3\Sigma^-$	−0.47	$1\sigma^2 2\sigma^2 3\sigma \bar{1}\pi_x 1\pi_y (1\delta_{x^2-y^2})$
	−0.47	$1\sigma^2 2\sigma^2 3\sigma 1\pi_x \bar{1}\pi_y (1\delta_{x^2-y^2})$
	0.47	$1\sigma^2 2\sigma^2 \bar{3}\sigma 1\pi_x 1\pi_y (1\delta_{x^2-y^2})$
	0.47	$1\sigma^2 2\sigma^2 3\sigma 1\pi_x 1\pi_y (1\delta_{x^2-y^2})$
$1^5\Delta$ (A_1)	0.95	$1\sigma^2 2\sigma^2 3\sigma 1\pi_x 1\pi_y 1\delta_{xy}$
$3^3\Pi$ (B_1)	0.80	$1\sigma^2 2\sigma 3\sigma^2 1\pi_x 1\pi_y^2$
$2^3\Delta$ (A_2)	0.82	$1\sigma^2 2\sigma 1\pi_x^2 1\pi_y^2 1\delta_{xy}$
$2^1\Delta$ (A_2)	−0.58	$1\sigma^2 \bar{2}\sigma 1\pi_x^2 1\pi_y^2 1\delta_{xy}$
	0.58	$1\sigma^2 2\sigma 1\pi_x^2 1\pi_y^2 \bar{1}\delta_{xy}$
$1^5\Pi$ (B_1)	−0.64	$1\sigma^2 2\sigma 3\sigma 1\pi_x 1\pi_y^2 (1\delta_{x^2-y^2})$
	0.64	$1\sigma^2 2\sigma 3\sigma 1\pi_x^2 1\pi_y 1\delta_{xy}$
$1^5\Phi$ (B_1)	0.66	$1\sigma^2 2\sigma 3\sigma 1\pi_x 1\pi_y^2 (1\delta_{x^2-y^2})$
	0.66	$1\sigma^2 2\sigma 3\sigma 1\pi_x^2 1\pi_y 1\delta_{xy}$

^a Only one component under C_{2v} symmetry is listed for Π , Δ , and Φ states. The respective irreducible representations are provided in parentheses.

^b All the configuration interaction coefficients that are larger than 0.30 of corresponding natural orbital representations are listed. ^c β and α -spin electrons are specified with and without bars over the spatial orbital.

is true where the r_e of $\text{HfN}^+(\text{X}^1\Sigma^+)$ is ~ 0.04 Å shorter than that of $\text{HfN}(\text{X}^2\Sigma^+)$ at all the utilized theoretical approaches (Tables 2



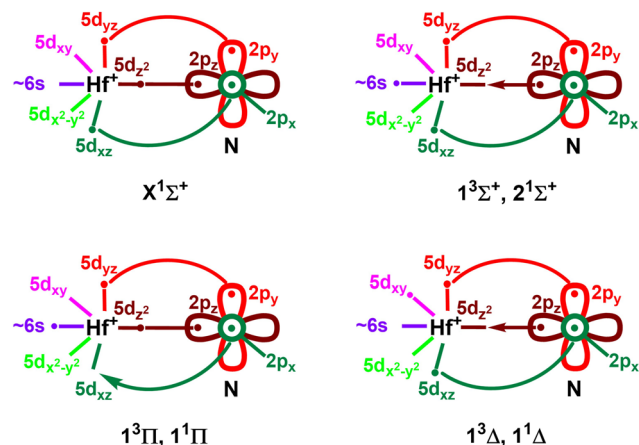


Fig. 7 Proposed vbL diagrams for the seven lowest energy electronic states of HfN^+ . In all cases, the 2s orbital of nitrogen is doubly occupied and not shown for clarity. See Table 3 for their exact electronic configurations.

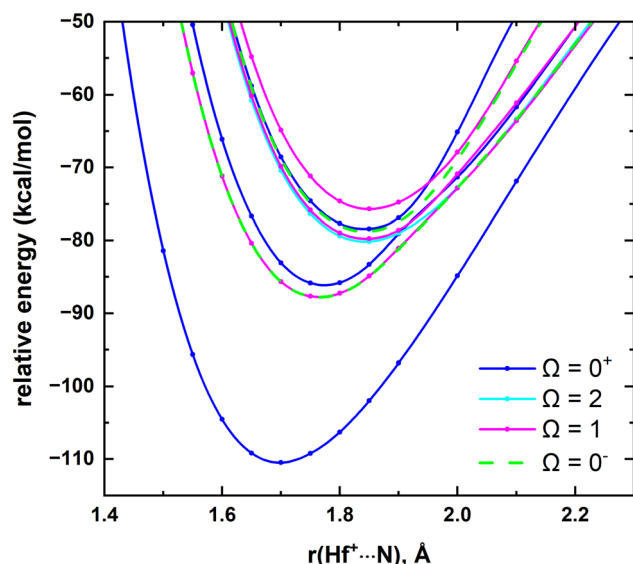


Fig. 8 MRCI spin-orbit coupling curves resulting from $X^1\Sigma^+$, $1^3\Sigma^+$, $2^1\Sigma^+$, $1^3\Pi$, and $1^1\Pi$ electronic states of HfN^+ as a function of $\text{Hf}^+\cdots\text{N}$ distance [$r(\text{Hf}^+\cdots\text{N})$, Å]. The relative energies are referenced to the lowest energy spin-orbit curve at $r = 12$ Å, which is set to 0 kcal mol $^{-1}$. The $\Omega = 0^+$, $\Omega = 2$, $\Omega = 1$, and $\Omega = 0^-$ curves are shown in blue, cyan, pink, and green, respectively. See Fig. 6 for the PECs of their parent $X^1\Sigma^+$, $1^3\Sigma^+$, $2^1\Sigma^+$, $1^3\Pi$, and $1^1\Pi$ states.

and 4). Among all the studied electronic states of HfN^+ the $X^1\Sigma^+$ ground state has the shortest r_e (Table 4). Notice that in the $X^1\Sigma^+$ state the 2σ , $1\pi_x$, and $1\pi_y$ bonding orbitals host six electrons in total which accounts for its triple bonded character. In all excited electronic states of HfN^+ these three bonding orbitals carry either five or four electrons, which rationalizes the comparatively longer r_e of excited states compared to the $X^1\Sigma^+$. Recall that for all the states of HfN , MRCI+Q predicted r_e are longer than the MRCI values. This trend does not translate to the states of HfN^+ , where the MRCI+Q r_e of HfN^+

Table 4 Dissociation energy with respect to ground state fragments (D_e , kcal mol $^{-1}$), bond length (r_e , Å), excitation energy (T_e , cm $^{-1}$), harmonic vibrational frequency (ω_e , cm $^{-1}$), and anharmonicity ($\omega_e x_e$, cm $^{-1}$) of low-lying states of HfN^+

State	Method ^a	D_e	r_e	T_e	ω_e	$\omega_e x_e$
$X^1\Sigma^+$	MRCI	112.45	1.697	—	965	6.6
	MRCI-SOC ($\Omega = 0^+$)	110.48	1.698	—	955	6.5
	MRCI+Q	115.71	1.695	—	982	5.8
	CCSD(T)	115.29	1.693	—	992	5.5
	QZ-C-CCSD(T)	117.18	1.674	—	1007	6.3
	5Z-C-CCSD(T)	119.47	1.672	—	1013	6.2
	CBS-C-CCSD(T)	120.56	1.671	—	1017	6.2
	DFT/B3LYP ²⁹	91.55	1.720	—	994	—
$1^3\Sigma^+$	MRCI	89.63	1.764	7984	921	3.8
	MRCI-SOC ($\Omega = 0^-$)	87.78	1.766	7939	920	7.0
	MRCI-SOC ($\Omega = 1$)	87.75	1.765	7950	922	6.8
	MRCI+Q	92.29	1.762	8191	934	4.0
	CCSD(T)	91.24	1.761	8410	954	3.7
	QZ-C-CCSD(T)	95.19	1.739	7690	975	3.6
	5Z-C-CCSD(T)	96.79	1.737	7932	978	3.6
	—	—	—	—	—	—
$2^1\Sigma^+$	MRCI	87.89	1.774	8591	985	3.5
	MRCI-SOC ($\Omega = 0^+$)	86.13	1.774	8517	928	11.7
	MRCI+Q	90.71	1.773	8745	990	3.3
	—	—	—	—	—	—
$1^3\Pi$	MRCI	81.86	1.845	10 700	836	5.1
	MRCI-SOC ($\Omega = 2$)	80.16	1.843	10 605	839	5.0
	MRCI-SOC ($\Omega = 1$)	79.75	1.845	10 749	866	4.1
	MRCI-SOC ($\Omega = 0^-$)	78.76	1.843	11 094	904	1.1
	MRCI-SOC ($\Omega = 0^+$)	78.42	1.842	11 215	911	4.4
	MRCI+Q	83.64	1.845	11 216	841	5.2
	CCSD(T)	81.95	1.840	11 661	852	3.6
	QZ-C-CCSD(T)	84.70	1.820	11 360	862	3.6
$1^1\Pi$	5Z-C-CCSD(T)	86.24	1.818	11 622	866	3.5
	MRCI	78.62	1.829	11 834	875	6.7
	MRCI-SOC ($\Omega = 1$)	75.68	1.850	12 171	890	1.2
	MRCI+Q	80.55	1.829	12 295	891	6.6
$1^3\Delta$	MRCI	66.80	1.783	15 968	903	5.9
	MRCI+Q	69.11	1.779	16 298	901	4.3
	CCSD(T)	68.49	1.775	16 366	916	3.5
	QZ-C-CCSD(T)	72.01	1.751	15 799	936	3.4
	5Z-C-CCSD(T)	73.92	1.749	15 929	939	3.4
$1^1\Delta$	MRCI	65.92	1.791	16 274	901	5.9
	MRCI+Q	68.19	1.787	16 619	894	4.7
$1^3\Phi$	MRCI	60.27	1.865	18 250	766	3.3
	MRCI+Q	61.86	1.864	18 834	772	3.9
$1^1\Phi$	MRCI	60.10	1.833	18 310	718	11.2
	MRCI+Q	61.74	1.833	18 876	732	11.5
$2^3\Pi$	MRCI	59.27	1.861	18 601	780	3.2
	MRCI+Q	60.98	1.861	19 142	784	3.7
$2^1\Pi$	MRCI	54.32	1.833	20 334	724	2.8
	MRCI+Q	56.16	1.833	20 825	735	2.8
$1^3\Sigma^-$	MRCI	47.99	2.054	22 545	614	3.3
	MRCI+Q	50.76	2.051	22 716	618	3.0
$1^5\Delta$	MRCI	44.15	2.068	23 889	600	2.9
	MRCI+Q	45.26	2.068	24 638	601	3.0
$3^3\Pi$	MRCI	41.38	1.947	24 860	728	2.2
	MRCI+Q	44.68	1.946	24 842	733	2.5
$2^3\Delta$	MRCI	40.82	2.050	25 053	874	10.1
	MRCI+Q	42.16	2.061	25 724	894	9.7

Table 4 (continued)

State	Method ^a	D_e	r_e	T_e	ω_e	$\omega_e x_e$
$2^1\Delta$	MRCI	40.04	2.072	25 327	989	18.5
	MRCI+Q	41.20	2.072	26 059	982	18.7
$1^5\Pi$	MRCI	36.25	1.965	26 654	709	4.1
	MRCI+Q	37.70	1.966	27 283	702	4.3
$1^5\Phi$	MRCI	35.76	1.965	26 824	708	4.1
	MRCI+Q	37.20	1.966	27 460	702	4.0

^a Davidson corrected MRCI is denoted by MRCI+Q. For all MRCI, MRCI+Q, and CCSD(T) calculations cc-pVQZ-PP (60ECP) of Hf and aug-cc-pVQZ of N basis set was applied. The $5s^25p^6$ (of Hf) core electrons correlated CCSD(T) calculations are labeled as XZ-C-CCSD(T) and the appropriate weighted-core cc-pwCVXZ-PP (60ECP) basis set of Hf was used (X = Q, 5). The MRCI findings of Ω states of five lowest electronic states of HfN⁺ are listed in the MRCI-SOC rows.

are either longer, shorter, or identical to the MRCI r_e (Table 4). Similar to the HfN($X^2\Sigma^+$), the spin-orbit mixing of the HfN⁺($X^1\Sigma^+$) is minor (ESI,[†] Table S4) and the r_e of the HfN⁺($X^1\Sigma^+$) is almost identical to the r_e of HfN⁺($X^1\Sigma_0^+$). Similarly, the r_e values of the parent electronic states $1^3\Sigma^+$, $2^1\Sigma^+$, and $1^3\Pi$ are either the same or nearly identical to their spin-orbit products (Table 4). For all states, the MRCI+Q predicted T_e are ~ 150 – 750 cm^{−1} higher than the MRCI T_e except for the $3^3\Pi$ state which has an 18 cm^{−1} lower MRCI+Q T_e compared to the MRCI T_e (Table 4). Importantly, this trend was also maintained by all but one excited state of HfN (Table 2). The spin-orbit effects decreased the first T_e value of HfN⁺ by 45 cm^{−1} (*i.e.*, 7984 *versus* 7939 cm^{−1}). The energy difference between $\Omega = 0^-$ and 1 products of the $1^3\Sigma^+$ is only 11 cm^{−1}. Similar to the $1^3\Sigma^+$ case, the spin-orbit couplings decreased T_e of the $2^1\Sigma^+$ (8591 *versus* 8517 cm^{−1}; see Table 4). The $\Omega = 2, 1, 0^-$, and 0^- components of the $1^3\Pi$ span between 10 605–11 215 cm^{−1}, where the T_e of only $\Omega = 2$ state is lower compared to the T_e of the original $1^3\Pi$ (Table 4).

The DFT/B3LYP $\omega_e = 994$ cm^{−1} value of the Hong *et al.*, is in better harmony with our ground state ω_e values and is almost identical to the CCSD(T) ω_e .²⁹ For all single-reference states the coupled cluster approaches predicted slightly larger ω_e values compared to the MRCI and MRCI+Q ω_e values (Table 4). For the ground state, the CBS extrapolation only increased the ω_e by 4 cm^{−1} compared to the 5Z-C-CCSD(T). The $\omega_e x_e$ of the CBS-C-CCSD(T) and 5Z-C-CCSD(T) are identical (6.2 cm^{−1}). The ω_e and $\omega_e x_e$ values of several low-lying spin-orbit curves are listed in Table 4.

The MRCI DMCs of the five most stable electronic states of HfN⁺ are given in ESI,[†] Fig. S1. The μ values of the single-reference $X^1\Sigma^+$, $1^3\Pi$, and $1^3\Sigma^+$ at the CCSD(T) level are -6.20 , -4.23 , and -3.51 D, respectively. Similar to HfN, the CCSD(T) μ values of HfN⁺ were calculated at the CCSD(T) r_e values (Table 4). These values are in excellent agreement with the corresponding MRCI μ values. Specifically, the discrepancies between MRCI *versus* CCSD(T) values are less than 0.08 D. For the ground state, the DFT/B3LYP μ has been reported before as 6.18 D, which is in perfect harmony with our MRCI and CCSD(T) values.²⁹

IV. Conclusions

In conclusion, the current work reports PECs, electronic configurations, and D_e , T_e , ω_e , and $\omega_e x_e$ values of fourteen and eighteen electronic states of HfN and HfN⁺ respectively at the MRCI and MRCI+Q levels of theory. Single-reference electronic states were also analyzed under the CCSD(T) method. At CCSD(T) the effects of the basis set and core electrons on the predictions were also tested. The ground state of HfN is a $X^2\Sigma^+$ with $1\sigma^22\sigma^23\sigma^11\pi^4$ electron configuration. At the MRCI level, the spin-orbit effect accounted D_0 of HfN($X^2\Sigma^+$) is 124.86 kcal mol^{−1} which is in harmony with the recently reported D_0 of HfN by Merriles *et al.* [*i.e.*, 123.93(9) kcal mol^{−1}].³⁰ Unlike HfN($X^2\Sigma^+$), the ground state of HfN⁺($X^1\Sigma^+$) dissociates to excited state fragments [*i.e.*, Hf⁺(a^4F) + N(4S)] and bears a D_0 of 109.10 kcal mol^{−1} with respect to the ground state fragments. By detaching an electron from the 3σ orbital of the HfN($X^2\Sigma^+$), the ground state of HfN⁺($X^1\Sigma^+$) can be created and this IE is 7.401 eV at the CBS-C-CCSD(T) level. Similar single electron ionization from the $3\sigma^2$ of the first excited state of HfN($2^2\Sigma^+$) produces the first two excited states of HfN⁺($1^3\Sigma^+$ and $2^1\Sigma^+$), whereas that of HfN($1^2\Pi$) creates the third and fourth excited states of HfN⁺ (*i.e.*, $1^3\Pi$ and $1^1\Pi$). The D_e increased in the order of CCSD(T) < QZ-C-CCSD(T) < 5Z-C-CCSD(T) for both HfN and HfN⁺. The core electron correlation was found to shorten the bond distances. The ground state of each HfN($X^2\Sigma^+$) and HfN⁺($X^1\Sigma^+$) is triple bonded in nature and carries the shortest bond lengths compared to their excited states which carry bond orders less than 3. The CCSD(T) μ *versus* MRCI μ values vary by 0.2–0.5 D for the states of HfN but the discrepancies between the two levels for the states of HfN⁺ are less than 0.08 D. Overall, the results of this study are in harmony with the previously reported experimental values and are expected to serve as a guide for future experimental studies on HfN and HfN⁺.

Data availability

The data supporting this article have been included as part of the ESI.[†]

Conflicts of interest

There are no conflicts to declare.

Acknowledgements

The support of the Los Alamos National Laboratory (LANL) Laboratory Directed Research and Development program Project No. 20240737PRD1 is acknowledged. This research used resources provided by the Los Alamos National Laboratory Institutional Computing Program, which is supported by the U.S. Department of Energy National Nuclear Security Administration under Contract No. 89233218CNA000001. Dr. Nuno M. S. Almeida is thanked for the useful discussions about spin-orbit coupling effects.



References

- 1 J. F. Harrison, *Chem. Rev.*, 2000, **100**, 679–716.
- 2 E. E. Claveau and E. Miliordos, *Phys. Chem. Chem. Phys.*, 2021, **23**, 21172–21182.
- 3 I. R. Ariyaratna and E. Miliordos, *Phys. Chem. Chem. Phys.*, 2018, **20**, 12278–12287.
- 4 N. M. S. Almeida, I. R. Ariyaratna and E. Miliordos, *J. Phys. Chem. A*, 2019, **123**, 9336–9344.
- 5 I. R. Ariyaratna, N. M. S. Almeida and E. Miliordos, *Phys. Chem. Chem. Phys.*, 2020, **22**, 16072–16079.
- 6 I. R. Ariyaratna and E. Miliordos, *Phys. Chem. Chem. Phys.*, 2021, **23**, 1437–1442.
- 7 I. R. Ariyaratna, C. Duan and H. J. Kulik, *J. Chem. Phys.*, 2022, **156**, 184113.
- 8 B. Gao, X. Li, K. Ding, C. Huang, Q. Li, P. K. Chu and K. Huo, *J. Mater. Chem. A*, 2019, **7**, 14–37.
- 9 D. D. Kumar, N. Kumar, S. Kalaiselvam, S. Dash and R. Jayavel, *Surf. Interfaces*, 2017, **7**, 74–82.
- 10 M. Kommer, T. Sube, A. Richter, M. Fenker, W. Schulz, B. Hader and J. Albrecht, *Surf. Coat. Technol.*, 2018, **333**, 1–12.
- 11 J. Peng and R. Zierold, *Encyclopedia of Condensed Matter Physics*, 2024, pp. 716–728, DOI: [10.1016/b978-0-323-90800-9.00206-7](https://doi.org/10.1016/b978-0-323-90800-9.00206-7).
- 12 X. Peng, C. Pi, X. Zhang, S. Li, K. Huo and P. K. Chu, *Sustainable Energy Fuels*, 2019, **3**, 366–381.
- 13 Z. Meng, S. Zheng, R. Luo, H. Tang, R. Wang, R. Zhang, T. Tian and H. Tang, *Nanomater.*, 2022, **12**, 2660.
- 14 W. Qi, Z. Cheng, S. Liu and M. Yang, *Catal. Sci. Technol.*, 2023, **13**, 6864–6877.
- 15 Z. Cheng, W. Qi, C. H. Pang, T. Thomas, T. Wu, S. Liu and M. Yang, *Adv. Funct. Mater.*, 2021, **31**, 2100553.
- 16 X. Dou, H. Han, G. Zhai and B. Suo, *Int. J. Quantum Chem.*, 2011, **111**, 3378–3384.
- 17 A. Farhat and S. N. Abdul-Al, *J. Comput. Chem.*, 2015, **36**, 1252–1258.
- 18 S. R. Langhoff and C. W. Bauschlicher, *J. Mol. Spectrosc.*, 1990, **143**, 169–179.
- 19 A. Nils and M. Boris, *Phys. Scr.*, 2000, **62**, 417.
- 20 I. Shim and K. A. Gingerich, *J. Mol. Struct.*, 1999, **460**, 123–136.
- 21 A. C. Borin and J. P. Gobbo, *J. Phys. Chem. A*, 2009, **113**, 12421–12426.
- 22 R. S. Ram, J. Liévin and P. F. Bernath, *J. Chem. Phys.*, 1998, **109**, 6329–6337.
- 23 R. Du, B. Suo, H. Han, Y. Lei and G. Zhai, *Int. J. Quantum Chem.*, 2013, **113**, 2464–2470.
- 24 K. A. Gingerich, *J. Chem. Phys.*, 1968, **49**, 19–24.
- 25 F. J. Kohl and C. A. Stearns, *J. Phys. Chem.*, 1973, **78**, 273–274.
- 26 T. C. Devore and T. N. Gallaher, *J. Chem. Phys.*, 1979, **70**, 3497–3501.
- 27 R. S. Ram and P. F. Bernath, *J. Mol. Spectrosc.*, 1997, **184**, 401–412.
- 28 G. P. Kushto, P. F. Souter, G. V. Chertihin and L. Andrews, *J. Chem. Phys.*, 1999, **110**, 9020–9031.
- 29 B. Hong, L. Cheng, M. Y. Wang and Z. J. Wu, *Mol. Phys.*, 2010, **108**, 25–33.
- 30 D. M. Merriles, A. S. Knapp, Y. Barrera-Casas, A. Sevy, J. J. Sorensen and M. D. Morse, *J. Chem. Phys.*, 2023, **158**, 084308.
- 31 H. J. Werner, P. J. Knowles, G. Knizia, F. R. Manby and M. Schütz, *Wiley Interdiscip. Rev.: Comput. Mol. Sci.*, 2011, **2**, 242–253.
- 32 H. J. Werner, P. J. Knowles, F. R. Manby, J. A. Black, K. Doll, A. Hesselmann, D. Kats, A. Kohn, T. Korona, D. A. Kreplin, Q. Ma, T. F. Miller, 3rd, A. Mitrushchenkov, K. A. Peterson, I. Polyak, G. Rauhut and M. Sibaev, *J. Chem. Phys.*, 2020, **152**, 144107.
- 33 H.-J. Werner and P. J. Knowles, *et al.*, *MOLPRO, version 2023.2, a package of ab initio programs*, see <https://www.molpro.net>.
- 34 H.-J. Werner and P. J. Knowles, *J. Chem. Phys.*, 1988, **89**, 5803–5814.
- 35 P. J. Knowles and H.-J. Werner, *Chem. Phys. Lett.*, 1988, **145**, 514–522.
- 36 K. R. Shamasundar, G. Knizia and H. J. Werner, *J. Chem. Phys.*, 2011, **135**, 054101.
- 37 R. A. Kendall, T. H. Dunning and R. J. Harrison, *J. Chem. Phys.*, 1992, **96**, 6796–6806.
- 38 D. Figgen, K. A. Peterson, M. Dolg and H. Stoll, *J. Chem. Phys.*, 2009, **130**, 164108.
- 39 H.-J. Werner and P. J. Knowles, *J. Chem. Phys.*, 1985, **82**, 5053–5063.
- 40 P. J. Knowles and H.-J. Werner, *Chem. Phys. Lett.*, 1985, **115**, 259–267.
- 41 D. A. Kreplin, P. J. Knowles and H. J. Werner, *J. Chem. Phys.*, 2019, **150**, 194106.
- 42 D. A. Kreplin, P. J. Knowles and H. J. Werner, *J. Chem. Phys.*, 2020, **152**, 074102.
- 43 K. Raghavachari, G. W. Trucks, J. A. Pople and M. Head-Gordon, *Chem. Phys. Lett.*, 1989, **157**, 479–483.
- 44 A. Kramida, Y. Ralchenko and J. Reader, *NIST Atomic Spectra Database (Version 5.3)*, National Institute of Standards and Technology, Gaithersburg, MD, 2015, <https://physics.nist.gov/asd>.
- 45 S. Bhattacharyya and J. F. Harrison, *Comput. Theor. Chem.*, 2022, **1216**, 113853.
- 46 I. R. Ariyaratna, Y. Cho, C. Duan and H. J. Kulik, *Phys. Chem. Chem. Phys.*, 2023, **25**, 26632–26639.
- 47 G. Knizia, *J. Chem. Theory Comput.*, 2013, **9**, 4834–4843.
- 48 I. R. Ariyaratna and E. Miliordos, *J. Quant. Spectrosc. Radiat. Transfer*, 2020, **255**, 107265.
- 49 N. M. S. Almeida, I. R. Ariyaratna and E. Miliordos, *Phys. Chem. Chem. Phys.*, 2018, **20**, 14578–14586.
- 50 M. C. Zammit, J. A. Leiding, J. Colgan, W. Even, C. J. Fontes and E. Timmermans, *J. Phys. B: At., Mol. Opt. Phys.*, 2022, **55**, 184002.
- 51 E. Gharib-Nezhad, A. R. Iyer, M. R. Line, R. S. Freedman, M. S. Marley and N. E. Batalha, *Astrophys. J., Suppl. Ser.*, 2021, **254**, 34.
- 52 J. Tennyson and S. N. Yurchenko, *Atoms*, 2018, **6**, 26.
- 53 S. N. Yurchenko, in *Chemical Modelling: Applications and Theory*, ed. M. Springborg and J.-O. Joswig, The Royal Society of Chemistry, 2013, ch. 7, pp. 183–228, DOI: [10.1039/9781849737241-00183](https://doi.org/10.1039/9781849737241-00183).
- 54 D. R. Lide, *CRC Handbook of Chemistry and Physics*, CRC Press, New York, 93rd edn, 2012.

